small structures
www.small-structures.com

Effects of Periodic Pore Ordering on Photocatalytic Hydrogen Generation with Mesoporous Semiconductor Oxides

*Tobias Weller, Jana Timm, Leonie Deilmann, Tobias S. Doerr, Christopher Greve, Alexey S. Cherevan, Peter A. Beaucage, Ulrich B. Wiesner, Eva M. Herzig, Dominik Eder, and Roland Marschall**

Crystalline and 3D continuous mesoporous quaternary $CsTaWO_6$ semiconductors are prepared with different degrees of long-range periodic order and local order, respectively, to investigate the influence of periodic pore order on the photocatalytic performance in hydrogen evolution of mesoporous photocatalysts. The degree of long-range order of the mesopores is changed by modifying the ratio between metal precursors and soft polymer template poly(isoprene-*b*-styrene-*b*-ethylene oxide) (PI-*b*-PS-*b*-PEO; ISO) in the sol–gel synthesis. Long-range periodic order is found to have no appreciable advantage compared with an only locally ordered continuous pore system. On the contrary, nonperiodically ordered mesopores result in higher activity toward photocatalytic hydrogen evolution, even with slightly smaller pore diameter and lower cumulative pore volume. Most importantly, it is shown that pore connectivity and heterogeneous pore systems in mesoporous photocatalysts play a major role for hydrogen evolution when other parameters are confirmed to be not rate limiting.

1. Introduction

Since the first reports on periodically ordered mesoporous silica materials by the Kresge group[1,2] and some earlier works, scientists all over the world have been fascinated by crystalline (periodic) pore ordering in such materials. This was facilitated by continuous developments in electron microscopy able to visualize such porosity on the nanometer scale.[3] Since then, long-range periodically ordered mesopores with a number of geometries have been reported, including 2D hexagonal, 3D cubic, 3D continuous gyroidal, and others, for a range of different materials including a vast number of (crystalline) oxides and hybrid materials.[4–7] Several synthesis approaches have been developed to prepare periodically ordered mesoporous materials, with hard and soft templating being the most ubiquitous ones.

Due to the fascination with long-range periodic pore order on the nanometer scale, scientists have been using such mesoporous materials for a range of different applications. This is

T. Weller, R. Marschall
Institute of Physical Chemistry
Justus-Liebig-University Giessen
35392 Giessen, Germany
E-mail: roland.marschall@uni-bayreuth.de

J. Timm, R. Marschall
Department of Chemistry
University of Bayreuth
95447 Bayreuth, Germany

L. Deilmann, A. S. Cherevan, D. Eder
Institut für Materialchemie
Technische Universität Wien
1060 Vienna, Austria

The ORCID identification number(s) for the author(s) of this article can be found under https://doi.org/10.1002/sstr.202200184.

DOI: 10.1002/sstr.202200184

T. S. Doerr
INM—Leibniz Institute for New Materials
Campus D2 2, 66123 Saarbrücken, Germany

T. S. Doerr
Department of Materials Science and Engineering
Saarland University
Campus D2 2, 66123 Saarbrücken, Germany

C. Greve, E. M. Herzig
Institute of Physics
Dynamics and Structure Formation—Herzig Group
University of Bayreuth
95447 Bayreuth, Germany

P. A. Beaucage, U. B. Wiesner
Materials Science and Engineering
Cornell University
14853 Ithaca, NY, USA

especially true in catalysis, since the large surface area, for example, of periodically ordered mesoporous oxides, can exhibit a higher number of active sites, especially after suitable postfunctionalization.[5] The advantages of a large surface area have been utilized in a number of other applications including sensing, proton conduction, and batteries.[8] In many cases where periodically ordered mesoporous materials have been achieved, the authors were inclined to link the improved performance with the degree to which the material displayed porosity and associated increased surface area. Nevertheless, to the best of our knowledge, no study is actually known that varies pore ordering of a material up to high-long-range ordering systematically and correlates the variation of pore ordering quantitatively with, for example, photocatalytic hydrogen evolution activity.

Some efforts to perform such studies have been reported, including a comparison of different types of ordered pore structures[9,10] or pore order.[11,12] However, since a review by Rolison[13] suggesting that periodic pore order in catalysis is not required, no systematic study has been reported on how periodic order in mesoporous materials affects catalytic applications, including photocatalysis.

The most probable reason for the lack of such studies is that it is experimentally challenging to vary solely the degree of periodic pore order, for example, of a mesoporous oxide, without changing other important material parameters, like the crystallite size, pore wall thickness, surface area, pore diameter, or pore wall surface chemistry, the latter being easily affected using different types of templates (e.g., using polymer or silica spheres as templates). The parameter easiest to cope with from this list likely is surface area: If all other parameters could be fixed, the resulting performance could be normalized to the accessible surface area,[14] while still making it possible to investigate the influence of the degree of mesopore order.

In earlier works, P123-derived nonordered mesoporous $CsTaWO_6$ samples were hinting at a larger pore size being beneficial compared with small and narrow pores for photocatalytic hydrogen evolution due to presumed improved mass transport in the larger pores.[15] Hard-templating approaches for $CsTaWO_6$ led to the same conclusion.[16] Motivated by these findings, we showed earlier that the triblock terpolymer poly (isoprene-*b*-styrene-*b*-ethylene oxide) (PI-*b*-PS-*b*-PEO; ISO) can be used for the preparation of a phase-pure and 3D cocontinuous periodically ordered mesoporous quaternary $CsTaWO_6$ semiconductor for photocatalytic hydrogen generation with cubic alternating gyroid morphology.[17]

Aiming for an experimental study on the impact of periodic mesopore order on photocatalytic performance, here we demonstrate improved synthesis control of this interesting semiconductor. By varying the amount of templating polymer ISO relative to inorganic precursors, as well as adjusting other synthetic parameters, we are able to control major physicochemical characteristics of the resulting mesoporous network. We show the preparation of a series of mesoporous $CsTaWO_6$ powders with large pore diameters that differ mainly in the degree of long-range periodic mesopore ordering, without significantly changing crystallite size in the pore walls or accessible surface area. Utilizing the resulting complex oxides as photocatalysts for sacrificial hydrogen evolution reaction (HER), we experimentally demonstrate that the degree of pore connectivity in mesoporous photocatalysts is the main factor controlling liquid-phase photocatalysis when other parameters are kept non rate-limiting.

2. Results and Discussion

2.1. Material Characterization

SEM images of ISO-derived mesoporous $CsTaWO_6$ with different precursor-to-polymer ratios and calcined at 550 °C are shown in **Figure 1**. These SEM images reveal increasing degrees of long-range mesopore disorder for samples with higher ISO ratio. Using 1000 µL of the precursor solution in the synthesis (see Experimental Section) instead of 250 µL essentially leads to a complete loss of long-range periodic order of the resulting mesoporous material, while preserving local order. This is expected as the polymer-to-precursor ratio is a well-known parameter to influence soft templating.[18]

Transmission electron microscopy (TEM) images in **Figure 2** corroborate the highly mesoporous nature of the ISO-derived mesoporous $CsTaWO_6$ photocatalysts and the high degree of

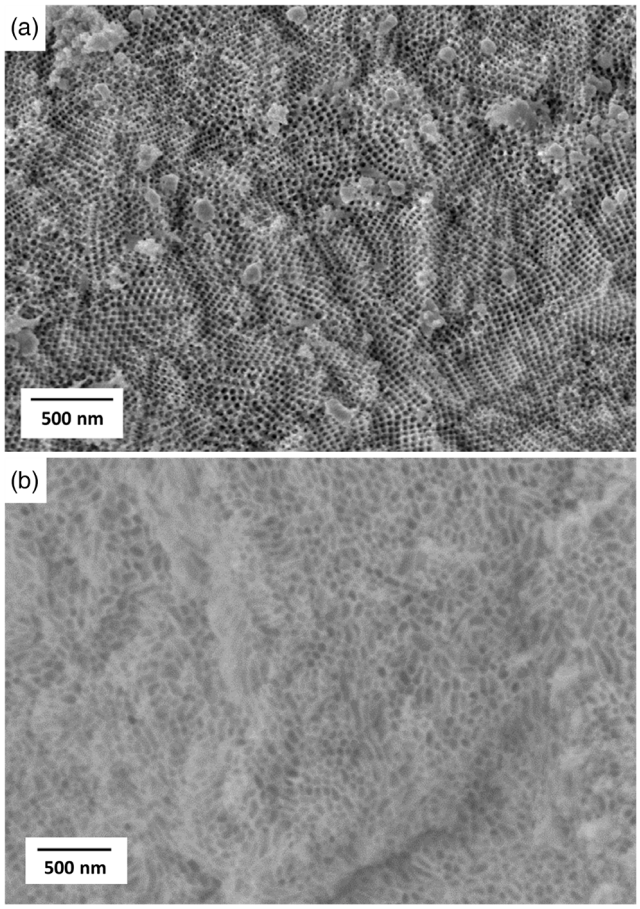

Figure 1. SEM images of ISO-derived mesoporous $CsTaWO_6$ with different precursor-to-polymer ratios, calcined at 550 °C, resulting in samples with different pore sizes and different degrees of long-range periodic pore order. The amounts of inorganic precursor solution added were a) 250 µL and b) 1000 µL, whereas the amount of polymer solution was kept constant at 2000 µL.

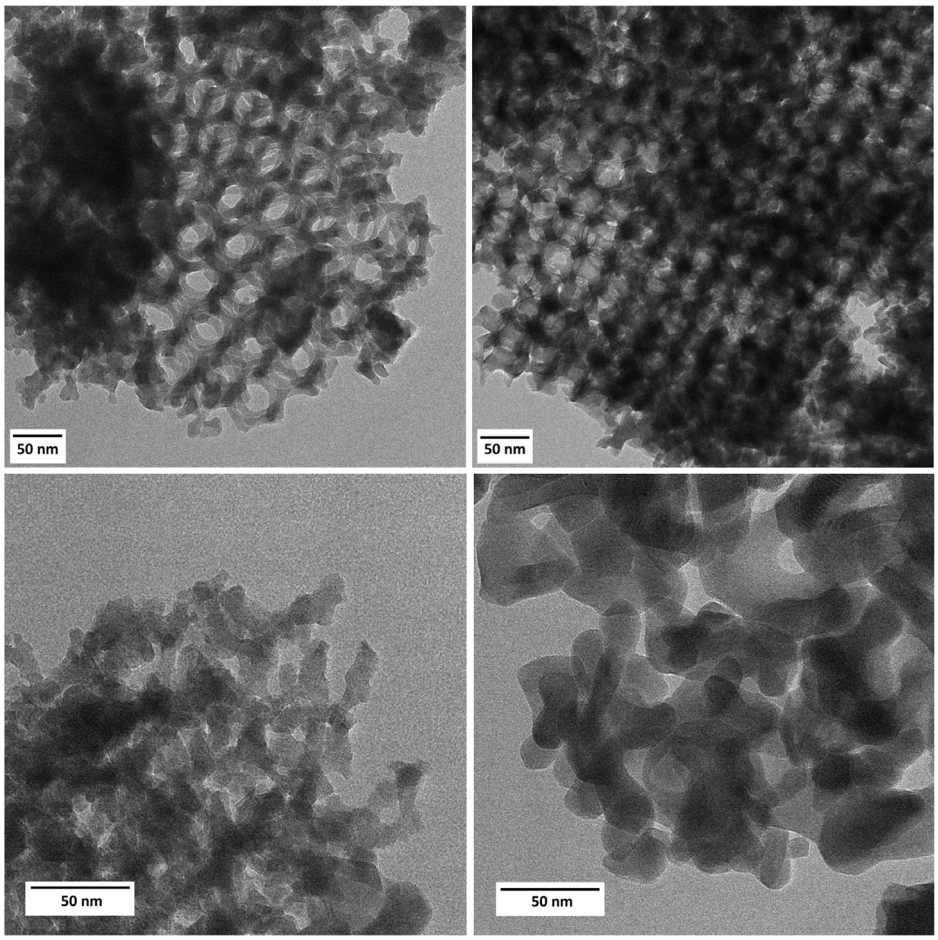

Figure 2. TEM images of ISO-derived mesoporous $CsTaWO_6$ derived from different precursor-to-polymer ratios, calcined at 550 °C (upper row) and 700 °C (lower row), resulting in long-range periodically ordered or disordered pore systems. The amounts of precursor solution were 250 µL (left) and 1000 µL (right), whereas the amount of polymer solution was kept constant at 2000 µL.

local periodic order when 550 °C calcination temperature is used (upper row images). Under these conditions, when moving from 250 to 1000 µL of inorganic precursor solution, the local periodic pore order is only weakly affected, consistent with SEM results. The situation changes substantially after calcination at 700 °C. Under this higher calcination temperature, while the porosity remains high, the local periodic pore order breaks down as expected due to sintering and crystal growth. High-resolution TEM images demonstrate that crystalline pore walls already emerge at a calcination temperature of 550 °C (Figure S1, Supporting Information).

Small-angle X-ray scattering (SAXS) examines a large sample volume of the bulk material and hence gives access to statistically averaged information on dominating length scales in the sampled volume. The SAXS results support the surface characterization carried out with TEM. The data on samples calcined at 550 °C for 1 h (**Figure 3**a) suggest that the long-range periodic mesoscale order of the mesoporous $CsTaWO_6$ derived from 250 µL inorganic precursor solutions is better developed than that derived from the 1000 µL amount, as the scattering peaks are much less smeared out. This is consistent with SEM results in Figure 1. Moreover, with more inorganic precursor, the lowest q peak shifts to higher scattering vector q, indicating a smaller lattice size and associated mesopores, consistent with TEM results shown in Figure 2 (upper row). SAXS results of samples from different amounts of inorganic precursor in their synthesis and calcined at the higher temperature of 700 °C for 1 h (Figure 3b) show weak low q peaks at similar q values like their counterparts calcined at 550 °C, but with almost complete loss of higher q peaks. This suggests similar lattice parameters and at the same time a reduced long-range periodic order for both $CsTaWO_6$ samples treated at the higher temperature.

N_2 physisorption isotherms of samples derived at 550 °C are depicted in **Figure 4**a. Desorption branches were analyzed using the quenched solid density functional theory (QSDFT) model for carbons with slit/cylindrical pores (see Experimental Section). Using this model, fitting errors stayed below 2% for each sample. The resulting pore size distribution (PSD) for $CsTaWO_6$ materials calcined at 550 °C and using 250 µL inorganic precursor solution in the synthesis suggests large pore sizes with a maximum approximately around 50 nm.[17] For material derived from 1000 µL inorganic precursor solution calcined at the same

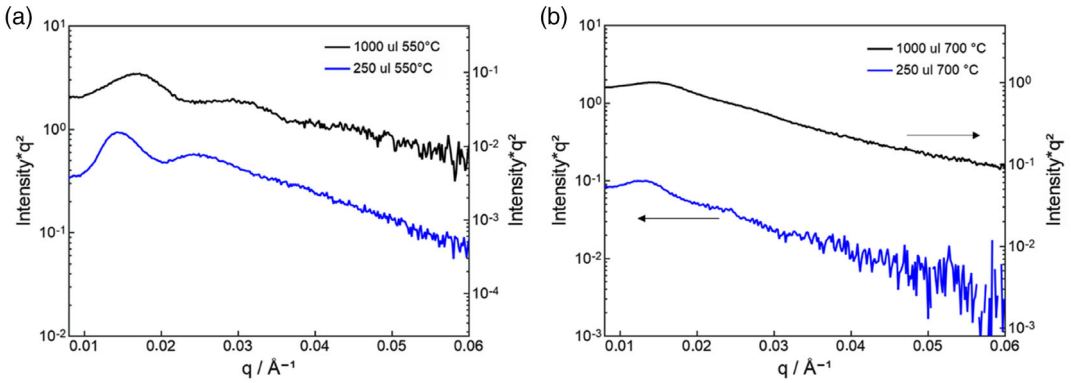

Figure 3. SAXS analysis of mesoporous $CsTaWO_6$ structure directed with terpolymer ISO, derived from either 250 µL (blue curves) or 1000 µL (black curves) inorganic precursor solutions, and a) calcined at 550 °C for 1 h (left side) or b) calcined at 700 °C for 1 h (right side).

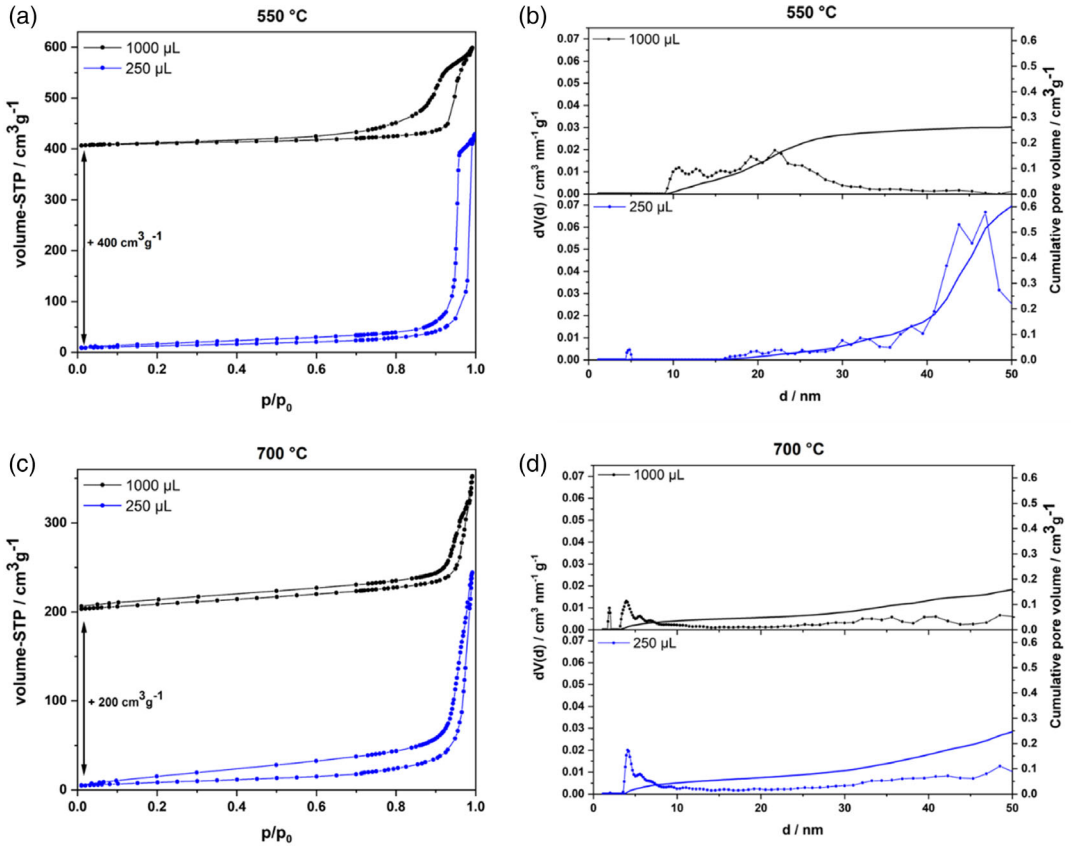

Figure 4. a) N_2 physisorption isotherms and b) PSDs calculated from the desorption branches of mesoporous $CsTaWO_6$ powders structure directed by terpolymer ISO with 250 µL (blue curves) or 1000 µL (black curves) inorganic precursor solutions and calcined at 550 °C for 1 h. c) N_2 physisorption isotherms and d) PSDs calculated from the desorption branches of mesoporous $CsTaWO_6$ powders structure directed by terpolymer ISO with 250 µL (blue curves) or 1000 µL (black curves) inorganic precursor solutions and calcined at 700 °C for 1 h. In (a) and (c), data are shifted vertically for samples derived from 1000 µL inorganic precursor solutions as indicated.

temperature, derived mesopore sizes were substantially smaller with a maximum around ≈25 nm, but more broadly distributed than for the 250 µL-derived oxide. These results corroborate earlier findings by SAXS, SEM, and TEM. Thus, using the applied QSDFT model for pore analysis is further validated. The cumulative pore volume of the sample derived from 250 µL inorganic is more than double that of the sample derived from 1000 µL inorganic (250 µL: 0.597 $cm^3 g^{-1}$; 1000 µL: 0.263 $cm^3 g^{-1}$). The specific surface area from BET analysis is 45.8 or 38.2 $m^2 g^{-1}$ for samples derived from 250 or 1000 µL

inorganic precursor, respectively. This suggests that despite differences in pore volume, accessible surface areas of the two samples remain close to each other.

Results of N_2 physisorption measurements and analysis of similarly prepared samples but calcined at 700 °C instead of 550 °C are depicted in Figure 4c,d, respectively. The N_2 physisorption isotherms still show a hysteresis, suggesting accessible pore systems. The PSDs from QSDFT model analysis of the desorption branches are markedly different from those of materials calcined at 550 °C, however. They show a much smaller maximum around ≈5 nm but also exhibit contributions at much larger pore sizes around 40–50 nm. With values around ≈0.2 $cm^3 g^{-1}$, the cumulative pore volumes are similar in both samples and lower than for samples calcined at 550 °C, in particular, as compared with the sample obtained from 250 µL inorganic precursor and calcination at 550 °C. The specific surface areas derived from BET analysis for the two materials calcined at 700 °C came out identical at 31.6 $m^2 g^{-1}$ and are lower than those of the oxides calcined at 550 °C.

In order to investigate whether the losses in local (Figure 2) and long-range order (Figure 3), as well as those in cumulative pore volume and accessible surface area (Figure 4), are associated with crystal growth, in particular when moving from 550 to 700 °C calcination temperature, detailed powder X-ray diffraction measurements and subsequent Rietveld refinements were carried out. Results are summarized in **Figure 5**. A fully crystalline, phase-pure product was received independent of the synthesis conditions. Crystallite sizes were estimated via Rietveld refinements for all samples. For oxides calcined at 550 °C (Figure 5a,c), as expected, a slightly higher average crystallite size was found for the sample derived from more inorganic precursors in the synthesis, that is, ≈12 versus 10 nm for materials from 1000 versus 250 µL inorganic precursor solution in the synthesis, respectively. For the higher calcination temperature of 700 °C (Figure 5b,d), analysis of both samples yielded the same crystallite sizes of around 16 nm. In all cases, the entire diffraction pattern could be refined well (crystallite sizes and discrepancy values are shown in Table S1, Supporting Information).

Raman spectra of all samples, including a reference sample prepared without the polymer template, always showed nine distinct Raman modes.[19] No substantial differences between materials obtained from different precursor amounts and different calcination temperatures could be detected (**Figure 6**a), corroborating results on phase purity from XRD pattern analysis (Figure 5). The bandgaps of all materials were determined *via* Tauc plot from diffuse reflectance UV–vis spectroscopy data, as illustrated in Figure 5b. All quaternary oxides displayed a bandgap of around 3.6 eV. This is consistent with values determined for a P123-derived mesoporous sample[15] and other $CsTaWO_6$ reference materials.[20] No quantum size effect could be observed in our measurements.

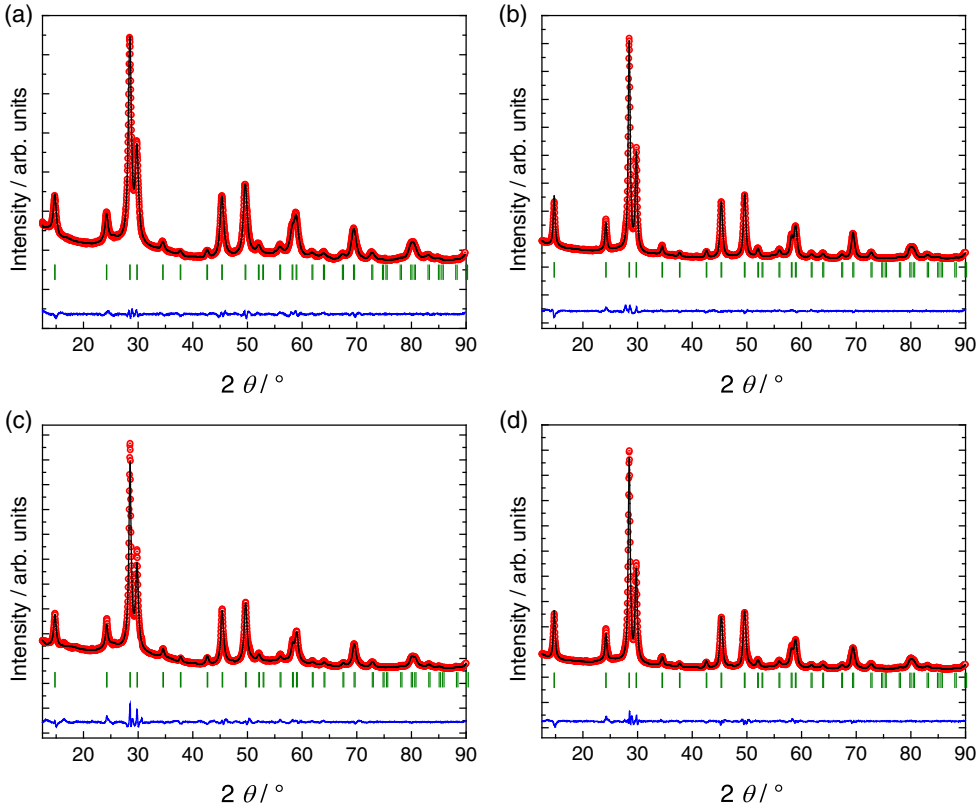

Figure 5. Rietveld refinements from XRD patterns of mesoporous $CsTaWO_6$ obtained from 250 µL inorganic precursor solution calcined at a) 550 °C and b) 700 °C and of mesoporous $CsTaWO_6$ obtained from 1000 µL inorganic precursor solution calcined at c) 550 °C and d) 700 °C.

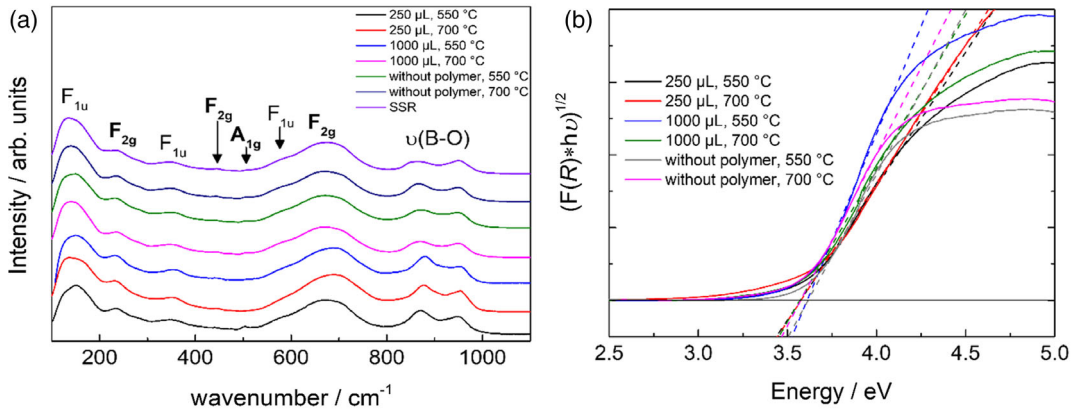

Figure 6. a) Raman and b) UV–vis spectra of mesoporous $CsTaWO_6$ structure directed by ISO from different inorganic precursor solutions and calcined at two different temperatures, as well as of reference samples with calcination steps at the same temperatures (SSR: solid-state reaction) but without ISO polymer (nonporous references).

2.2. Photocatalysis

Based on earlier reports on the application of $CsTaWO_6$ in photocatalysis, we tested the performance of our model materials toward solution-based HER.[14,21] We used methanol as a sacrificial agent, thereby taking its relatively small size into account that should not pose any diffusion limitations inherent to photocatalysis in mesoporous materials with small pores or larger organic reactants.

Results of hydrogen evolution performance (steady-state H_2 evolution rates) are depicted in **Figure 7** for samples derived from 250 or 1000 µL inorganic precursor solution in the synthesis and calcined at 550 °C. As described before, Rh as co-catalyst was deposited via in-situ photodeposition.[22] We presume that due to the addition of a liquid precursor in the dark, homogeneous deposition is achieved under stirring.

Figure 7a summarizes the hydrogen evolution rates for different amounts of Rh metal deposited on the two mesoporous $CsTaWO_6$ materials obtained from calcination at 550 °C. The results show higher performance for the material obtained from more inorganic precursor used in the synthesis. To account for the different surface areas of the materials, steady-state H_2 evolution rates were normalized per absolute surface area of photocatalysts present in the experiment. We believe that this normalization is valid, since the $CsTaWO_6$ photocatalysts prepared in this study were derived from similar soft-templating protocols, followed by the same calcination post-treatment, and thus should have similar surface chemistry.

It needs to be pointed out that relative to mesoporous $CsTaWO_6$ prepared from 1000 µL inorganic solution, the material obtained from 250 µL inorganic precursor solution shows better long-range periodic order (Figure 1 and 3), has larger pores, and larger cumulative pore volume (Figure 2 and 4) and therefore is expected to have more accessible pore surface area. Our H_2 evolution results in Figure 7a suggest, however, that these characteristics barely affect the photocatalytic activity, as the pores in both materials are large enough to eliminate potential diffusion limitations. Furthermore, the crystallite sizes, L_a, of our mesoporous materials are similar to those in the best-performing $CsTaWO_6$ nanoparticles, which is around

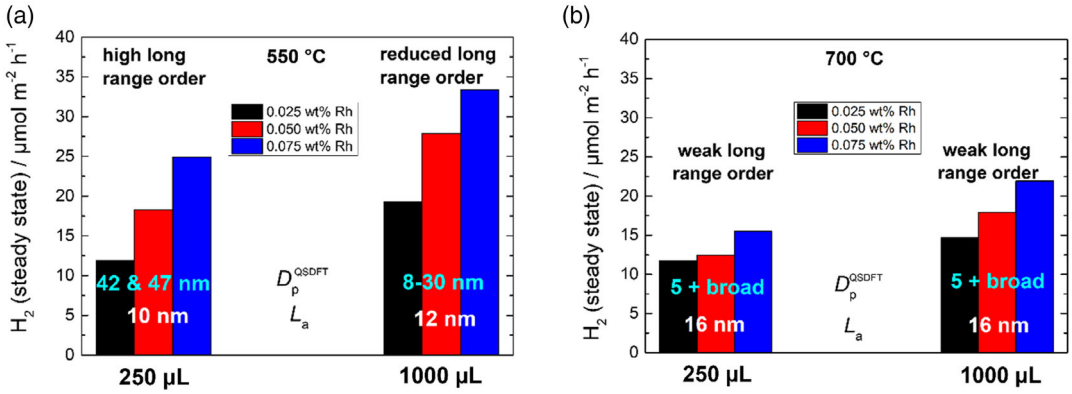

Figure 7. a) Photocatalytic steady-state hydrogen evolution rates normalized to surface area of mesoporous $CsTaWO_6$ samples prepared from 250 or 1000 µL inorganic precursor solution in the synthesis and calcination at 550 °C. Average crystallite sizes (L_a, white letters) from XRD, and pore diameter (D_p blue letters) from the physisorption measurements and quality of long-range order from SAXS are indicated on the respective histograms; b) after calcination at 700 °C.

13 nm.[23] Thus, this little difference should present no limitation for charge carrier separation as well, thus also excluding this process as a limiting factor for H_2 generation.

For comparison, Figure 7b shows the steady-state H_2 evolution rates for the samples calcined at 700 °C which are lower than for the samples calcined at 550 °C. These 700 °C-samples exhibit strongly reduced long-range periodic order (Figure 1 and 3), smaller and irregular pores, and lower cumulative pore volume (Figure 2 and 4). In contrast to the materials prepared with higher precursor amount (right side of Figure 7a,b), both samples calcined at 700 °C (Figure 7b) show significantly lower H_2 evolution rates than samples calcined at 550 °C. It is important to note that, although the crystallite size of the pore walls is slightly increased, it is still close to the optimum size reported earlier.[23] Thus the crystal size is representing no rate-limiting factor for charge carrier separation. In fact, one would expect an evolution rate increase for 700 °C calcination, as higher calcination temperatures usually heal oxygen defects that often represent major recombination centers in oxide-based photocatalysts including $CsTaWO_6$.[20] Interestingly, it seems that the lower cumulative pore volume and the strongly reduced long-range periodic order found for the 700 °C calcined samples counteract this defect healing and overall lead to reduced photocatalytic activity in comparison with the samples calcined at 550 °C.

In order to understand the fundamental impact of the pore characteristics in more detail, we conducted scanning physisorption measurements (**Figure 8**).[24] In particular, this method can reveal the pore connectivity of mesopores in a material, which is of key importance for diffusion and mass transport-related applications, for example, photocatalytic hydrogen generation. In addition, this technique also allows to differentiate between multiple pore systems in the same material.[25]

The desorption scanning method was used to investigate the gas desorption behavior within one pore depending on the pore characteristics and filling grade of its neighboring pores. In general, if the gas desorption behavior of a pore is dependent on the neighboring pores and their filling grade, the desorption branches of different isotherm scans intersect in only one point, at the p/p^0 value of the start/end of the hysteresis loop of the respective isotherm. If the gas desorption behavior of a pore is independent of the neighboring pores and their filling, the desorption branches of different isotherms show comparable hysteresis loops and comparable courses of their respective desorption branches. Furthermore, the PSD resulting from the different scans would be comparable with each other in the latter case.[26]

As shown in Figure 8a, the scanning isotherms for the mesoporous $CsTaWO_6$ photocatalyst obtained from 250 µL inorganic solution follow the shape of the initial isotherm from each starting point, indicating one independent pore system.[27–29] The resulting PSDs (Figure 8b) show this effect more clearly. The maxima of the PSDs for each scan display similar pore diameters, while only the intensity of the distribution and the

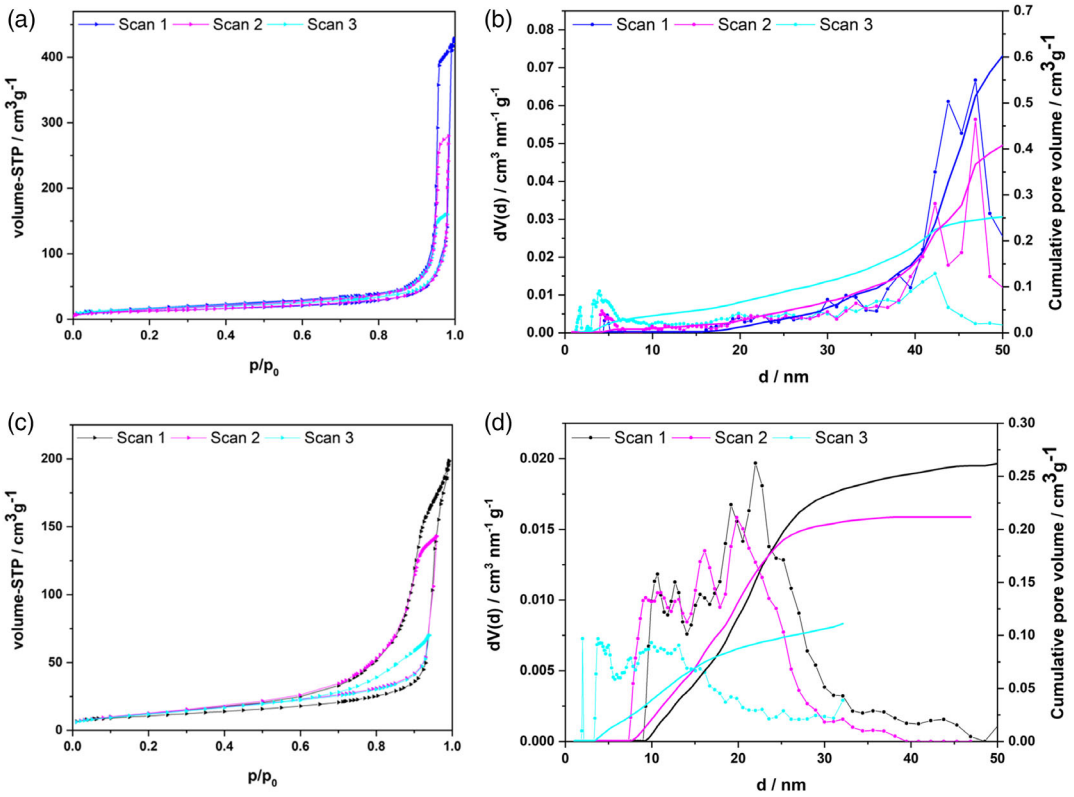

Figure 8. a) N_2 physisorption isotherm scanning curves of mesoporous $CsTaWO_6$ prepared from 250 µL inorganic solution and calcined at 550 °C, with b) the resulting PSD and cumulative pore volumes; c) N_2 physisorption isotherm scanning curves of mesoporous $CsTaWO_6$ prepared from 1000 µL inorganic solution and calcined at 550 °C, with d) respective PSC and cumulative pore volume.

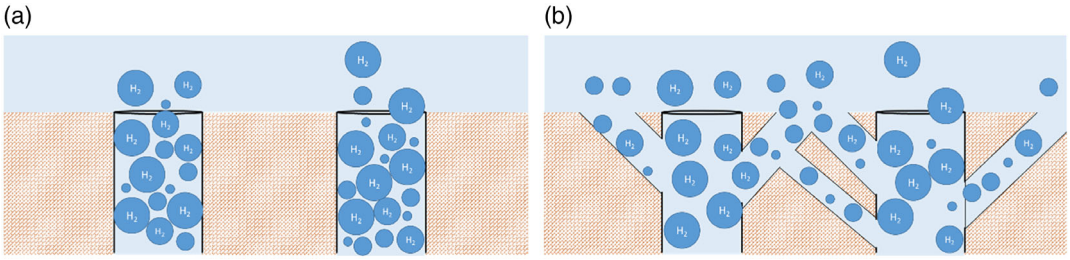

Figure 9. a) H_2 gas evolution (depicted are H_2 gas bubbles of different sizes) from an independent pore system, as present in mesoporous $CsTaWO_6$ prepared from 250 µL inorganic solution and calcined at 550 °C; compared with b) H_2 gas evolution from a heterogeneous pore system interconnected, as present in mesoporous $CsTaWO_6$ prepared from 1000 µL inorganic solution and calcined at 550 °C. In (b), different release pathways for H_2 gas bubbles are available, facilitating mass transport from the pore system.

cumulative pore volume is decreasing. This further underlines the presence of an ordered pore system in which the pores must be filled or emptied independently.

In contrast, the scanning isotherms of the mesoporous $CsTaWO_6$ prepared with higher precursor amount (Figure 8c) do not follow the shape of the initial isotherms at each starting point, indicating a heterogeneous pore system where filling or emptying pores depends on the neighboring pores. The analysis of the respective PSD for high precursor amount (Figure 8d) shows these differences more clearly. This observation suggests that the release of evolved gas bubbles in this mesoporous material is improved due to the possibility to choose different pore pathways (see **Figure 9**).

This faster gas release can also be responsible for the observed increased photocatalytic activity of the mesoporous $CsTaWO_6$ derived from 1000 µL precursor compared with the mesoporous $CsTaWO_6$ from 250 µL precursor. Therefore, despite its lower long-range order, lower cumulative pore volume, and smaller pore sizes, the presence of a heterogeneous intercorrelated pore system appears to be the crucial factor in the improvement of porous $CsTaWO_6$ for gas evolution here. Conclusively, the direct analysis of the filling or emptying behavior of porous materials plays a major role in predicting transport characteristics and (photo)catalytic performances in porous materials.

3. Conclusion

A set of model mesoporous $CsTaWO_6$ samples with different pore sizes and pore ordering degrees were prepared using the block copolymer ISO as the structure-directing agent. Scanning physisorption measurements revealed that the heterogeneity of the pore system as well as the intercorrelated pore connectivity can have a major influence on the activity of mesoporous materials for photocatalytic hydrogen evolution, when long-range pore ordering, cumulative pore volume, and crystallite sizes of pore walls are no more rate-limiting factors. In addition, short-range order of mesopores does seem to play a major role in mesoporous photocatalysts for hydrogen evolution, since calcination and breakdown of porosity resulted in lower hydrogen evolution rates per surface area. These results can be likely extended for similar applications in liquid-phase photo-, electro-, and acid–base catalysis using mesoporous systems.

4. Experimental Section

Materials: ISO synthesis and characterization were described in earlier work.[17,30,31] Metal precursor and solvents were dissolved separately, the ISO polymer in pure THF, and the precursors in abs. EtOH, starting with Cs_2CO_3. After 1 h of stirring, $TaCl_5$ was added and stirred for another 30 min. Finally, WCl_6 was added to the precursor solution, which immediately turned from colorless to orange/brown. The solution was stirred for another hour. Then, 2 mL of polymer solution was mixed together with varying volumes of inorganic precursor solution, with the exact ratio determining the degree of pore ordering (e.g., 250 µL led to long-range periodically ordered mesopores, 1000 µL to disordered mesopores). All solutions were then stirred for another 2 h. Solutions were finally transferred into a PTFE cup, each with a volume of 5 mL, and put on a heating plate at 40 °C under a glass dome to trigger slow evaporation-induced self-assembly (EISA). After solvent evaporation was complete, the PTFE cups were transferred into a small vacuum oven for final drying (Büchi glass oven B-585) by heating to 50 °C under vacuum for 24 h. The resulting pellet-like dark blue solids were calcined in air for 1 h at 550 or 700 °C resulting in white powders.

Characterization: Scanning electron microscopy (SEM) was performed on a Zeiss Merlin instrument. For TEM images, a 200 kV JEOL JEM-2200FS EFTEM was used equipped with Schottky FEG and In-Column Omega Energy filter from JEOL GmbH. Prior to each measurement, 1–2 mg of the sample was suspended in 1 mL of ethanol (AcrosOrganics, extra dry, 99.5%). Then, 4–8 µL of the suspension was dropped on a carbon film-coated Cu TEM grid (200 Mesh).

X-ray powder diffraction (XRPD) patterns were measured on an X'Pert PRO diffractometer from PANalytical Instruments (Cu Kα radiation, $\lambda = 1.5418$ Å) with an acceleration voltage of 40 kV and an emission current of 40 mA. Data were recorded in a step scan mode from 10° to 90° with a step size of 0.03°. For Rietveld refinement, FULLPROF 2.05 software and a modified Thompson–Cox–Hastings Pseudo–Voigt profile function were used. The quality of the fits was characterized through the weighted profile *R*-factor (R_{wp}) and the goodness of fit (χ^2).

SAXS measurements were carried out on a Xenocs Xeuss 3.0 (Xenocs, France) equipped with a copper source ($\lambda = 1.5418$ Å). Scattering images were detected on an Eiger2 R 1M detector (Dectris, Switzerland) with 1028 × 1062 pixels and a pixel size of 75 µm × 75 µm located 1.8 m from the sample (sample detector distance deducted via AgBeh calibration). The beam size was adjusted to 0.5 mm × 0.5 mm and each sample was measured for 48 h, with single-image exposure times of 4 h. The measured single SAXS images were masked around the direct beam to eliminate refraction effects resulting from the measurement container prior to azimuthal averaging and summation with the software XSACT 2.0 (Xenocs, France). The resulting 1D cuts were further corrected for background scattering from an empty sample container.

Raman spectroscopy was performed on a Senterra II Raman spectrometer from Bruker.

Nitrogen (N_2) physisorption analysis was performed at 77 K using an Anton Paar QuantaTec ASiQ-MP-MP-AG instrument (scanning curves) and an Anton Paar QUADRASORB evo surface area and pore size analyzer (standard isotherms). PSDs were calculated using the QSDFT[32] model for carbons with slit/cylindrical pores. We chose this kernel due to several reasons. First, the fitting of quaternary material systems is very difficult due to the assumptions which are made by the different fitting models. For example, nonlocal DFT (NLDFT) can only be used when having materials with homogenous surfaces,[33–36] but due to the composition of our material the surface could not be considered as homogeneous or smooth. That makes QSDFT[34,36] more suitable to use, because here inhomogeneities in the pore walls are taken into account. Second, the surface termination has also a huge impact on the fitting model, but there is no fitting model available for other metal oxides than silica or zeolites for QSDFT. Even the similarity of the silica/zeolitic surface and the surface of $CsTaWO_6$ is questionable. Therefore, we checked on the smallest fitting errors for all nitrogen physisorption measurements in this manuscript (including the hysteresis scans) and found that the chosen QSDFT kernel (carbon, slit/cylindrical pores) fit best with fitting errors with maximum of 2%. Specific surface areas were estimated by applying the Brunauer–Emmett–Teller (BET) model.[37] All samples were degassed in vacuum at 150 °C for at least 12 h prior to the measurements. Data evaluation was carried out with the program ASiQwin 4.0.

For the scanning isotherm technique, several isotherms were measured subsequently, with stepwise-reduced endpoints of the adsorption branch. Therefore, after the first full isotherm between 0 and 0.99 $p\,p^{-0}$, a second adsorption measurement was started immediately up to 0.97 $p\,p^{-0}$, followed by another desorption branch using this last data point as start. A third adsorption measurement was started immediately after the second adsorption measurement, but only up to 0.95 $p\,p^{-0}$, followed by the final desorption measurement.

A PerkinElmer Lambda 750 UV/Vis/NIR spectrometer, equipped with a Praying-Mantis mirror unit from Harrick, was used to record the diffuse reflectance with step size of 1 nm. A spectralon pellet was used as white standard. The spectra were converted into absorption spectra using Kubelka–Munk function; band gaps were estimated using Tauc plots.[38]

Hydrogen Evolution: 300 mg mesoporous photocatalyst was suspended in 600 mL of an aqueous methanol solution (10 vol%) and filled into a homemade inner irradiation-type glass reactor.[17] A 700 W Hg midpressure immersion lamp set to 50% (350 W, Peschl UV-Consulting) was used as a light source; the lamp was cooled to 10 °C with a double-walled quartz mantle using a thermostat (LAUDA RP845). Gas evolution was measured online using a mass spectrometer (Hiden HPR-20 Q/C). Argon 5.0 was used as carrier gas; the continuous gas flow was controlled by mass flow controller (Bronkhorst). The gas flow was set to 100 mL min^{-1}. All reactions were performed at 10 °C, and again the reactor cooled with a thermostat (LAUDA RP845). Before the photocatalytic reaction, the whole reactor system, with the photocatalyst included, was flushed with argon 5.0 for 1 h to remove any trace of air. Successive cocatalyst precursor (Na_3RhCl_6 (Aldrich)) addition for photodeposition was performed through a rubber sealing (without opening the reactor) after turning off the light source, to avoid prolonged intermediate argon flushing for air removal.

Supporting Information

Supporting Information is available from the Wiley Online Library or from the author.

Acknowledgements

Paul Gebhardt (TU Wien) and Christopher Simon (University Bayreuth) are acknowledged for additional transmission electron microscopy (TEM) measurements. T.W. and R.M. gratefully acknowledge funding in the Emmy-Noether program (MA 5392/3-1) of the German Research Foundation DFG and E.M.H. and C.G. the DFG support through TUM International Graduate School of Science and Engineering (IGSSE) and the Bavarian State Ministry of Science, Research and the Arts through the Collaborative Research Network "Solar Technologies go Hybrid." This work made use of DFG (INST 91/443-1) and the Cornell Center for Materials Research Shared Facilities supported through the NSF MRSEC program (DMR-1719875). P.A.B. was supported by the NSF GRFP program (DGE-1650441). U.B.W. thanks the National Science Foundation for support (DMR-1707836). The funding number for MRSEC program was changed post initial online publication.

Open Access funding enabled and organized by Projekt DEAL.

Conflict of Interest

The authors declare no conflict of interest.

Data Availability Statement

The data that support the findings of this study are available from the corresponding author upon reasonable request.

Keywords

hydrogen evolution reactions, mesopores, photocatalysis, pore ordering, scanning isotherms

Received: July 28, 2022
Revised: September 16, 2022
Published online: October 12, 2022

[1] J. S. Beck, J. C. Vartuli, W. J. Roth, M. E. Leonowicz, C. T. Kresge, K. D. Schmitt, C. T. W. Chu, D. H. Olson, E. W. Sheppard, S. B. McCullen, J. B. Higgins, J. L. Schlenker, *J. Am. Chem. Soc.* **1992**, *114*, 10834.
[2] C. T. Kresge, M. E. Leonowicz, W. J. Roth, J. C. Vartuli, J. S. Beck, *Nature* **1992**, *359*, 710.
[3] Y. Sakamoto, M. Kaneda, O. Terasaki, D. Y. Zhao, J. M. Kim, G. Stucky, H. J. Shin, R. Ryoo, *Nature* **2000**, *408*, 449.
[4] H. Tüysüz, F. Schüth, *Adv. Catal.* **2012**, *55*, 127.
[5] F. Hoffmann, M. Cornelius, J. Morell, M. Fröba, *Angew. Chem. Int. Ed.* **2006**, *45*, 3216.
[6] J. Lee, M. Christopher Orilall, S. C. Warren, M. Kamperman, F. J. DiSalvo, U. Wiesner, *Nat. Mater.* **2008**, *7*, 222.
[7] M. C. Orilall, U. Wiesner, *Chem. Soc. Rev.* **2011**, *40*, 520.
[8] X. Ji, K. T. Lee, L. F. Nazar, *Nat. Mater.* **2009**, *8*, 500.
[9] X. Deng, W. N. Schmidt, H. Tüysüz, *Chem. Mater.* **2014**, *26*, 6127.
[10] N. Dvoyashkina, C. F. Seidler, M. Wark, D. Freude, J. Haase, *Microporous Mesoporous Mater.* **2018**, *255*, 140.
[11] T. Grewe, X. Deng, C. Weidenthaler, F. Schüth, H. Tüysüz, *Chem. Mater.* **2013**, *25*, 4926.
[12] S. J. Reich, A. Svidrytski, A. Höltzel, J. Florek, F. Kleitz, W. Wang, C. Kübel, D. Hlushkou, U. Tallarek, *J. Phys. Chem. C* **2018**, *122*, 12350.
[13] D. R. Rolison, *Science* **2003**, *299*, 1698.
[14] A. S. Cherevan, L. Deilmann, T. Weller, D. Eder, R. Marschall, *ACS Appl. Energy Mater.* **2018**, *1*, 5787.
[15] T. Weller, J. Sann, R. Marschall, *Adv. Energy Mater.* **2016**, *6*, 1600208.
[16] M. Weiss, S. Waitz, R. Ellinghaus, T. Weller, R. Marschall, *RSC Adv.* **2016**, *6*, 79037.
[17] T. Weller, L. Deilmann, J. Timm, T. S. Dörr, P. A. Beaucage, A. S. Cherevan, U. B. Wiesner, D. Eder, R. Marschall, *Nanoscale* **2018**, *10*, 3225.
[18] N. D. Petkovich, A. Stein, *Chem. Soc. Rev.* **2013**, *42*, 3721.

[19] M. Mączka, A. V. Knyazev, A. Majchrowski, J. Hanuza, S. Kojima, *J. Phys. Condens. Matter* **2012**, *24*, 195902.
[20] L. Schwertmann, M. Wark, R. Marschall, *RSC Adv.* **2013**, *3*, 18908.
[21] A. S. Cherevan, S. Robbins, D. Dieterle, P. Gebhardt, U. Wiesner, D. Eder, *Nanoscale* **2016**, *8*, 16694.
[22] J. Soldat, R. Marschall, M. Wark, *Chem. Sci.* **2014**, *5*, 3746.
[23] T. Weller, L. Specht, R. Marschall, *Nano Energy* **2017**, *31*, 551.
[24] C. Simon, J. Timm, D. Tetzlaff, J. Jungmann, U.-P. Apfel, R. Marschall, *ChemElectroChem* **2021**, *8*, 227.
[25] K. A. Cychosz, R. Guillet-Nicolas, J. García-Martínez, M. Thommes, *Chem. Soc. Rev.* **2017**, *46*, 389.
[26] R. Cimino, K. A. Cychosz, M. Thommes, A. V. Neimark, *Colloids Surf. A Physicochem. Eng. Asp.* **2013**, *437*, 76.
[27] S. A. Kube, K. Turke, R. Ellinghaus, D. Wallacher, M. Thommes, B. M. Smarsly, *Langmuir* **2020**, *40*, 11996.
[28] E. Özkan, A. Hofmann, M. Votsmeier, W. Wang, X. Huang, C. Ku, F. Badaczewski, K. Turke, S. Werner, B. M. Smarsly, *Langmuir* **2021**, *37*, 2563.
[29] C. Schlumberger, M. Thommes, *Adv. Mater. Interfaces* **2021**, *8*, 2002181.
[30] M. A. Hillmyer, F. S. Bates, *Macromolecules* **1996**, *29*, 6994.
[31] J. Chatterjee, S. Jain, F. S. Bates, *Macromolecules* **2007**, *40*, 2882.
[32] A. V. Neimark, Y. Lin, P. I. Ravikovitch, M. Thommes, *Carbon* **2009**, *47*, 1617.
[33] M. Thommes, K. Kaneko, A. V. Neimark, J. P. Olivier, F. Rodriguez-Reinoso, J. Rouquerol, K. S. W. Sing, *Pure Appl. Chem.* **2015**, *87*, 1051.
[34] C. Schlumberger, M. Thommes, *Adv. Mater. Interfaces* **2021**, *8*, 2002181.
[35] J. N. Caguiat, D. W. Kirk, C. Q. Jia, *Carbon* **2014**, *72*, 47.
[36] J. Landers, G. Y. Gor, A. V. Neimark, *Colloids Surf. A Physicochem. Eng. Asp.* **2013**, *437*, 3.
[37] S. Brunauer, P. H. Emmett, E. Teller, *J. Am. Chem. Soc.* **1938**, *60*, 309.
[38] J. Tauc, R. Grigorovici, A. Vancu, *Phys. Status Solidi* **1966**, *15*, 627.